



Occurrence of both hydroxyl radical and surface oxidation pathways in N-doped layered nanocarbons for aqueous catalytic ozonation

Yuxian Wang^{a,b}, Lulu Chen^c, Chunmao Chen^b, Jiaxin Xi^c, Hongbin Cao^a, Xiaoguang Duan^d, Yongbing Xie^{a,*}, Weiyu Song^{c,*}, Shaobin Wang^d

^a Division of Environment Technology and Engineering, Institute of Process Engineering, Chinese Academy of Sciences, Beijing, 100190, China

^b State Key Laboratory of Petroleum Pollution Control, China University of Petroleum-Beijing, Beijing, 102200, China

^c State Key Laboratory of Heavy Oil Processing, China University of Petroleum-Beijing, 18 Fuxue Road, Beijing, 102249, China

^d School of Chemical Engineering, The University of Adelaide, Adelaide, SA, 5005, Australia



ARTICLE INFO

Keywords:

Metal-free catalysis
Catalytic ozonation
Nitrogen doping
Surface oxidation
Density functional theory (DFT)

ABSTRACT

Metal-free catalysts such as N-doped nanocarbons are sustainable alternatives to metal-based catalysts for the degradation of persistent organic pollutants (POPs), but cost-efficient methods are required for their large-scale synthesis. In this study, a facile and scalable strategy was established for synthesizing layered N-doped nanocarbons via the pyrolysis of β -cyclodextrin (β -CD) and melamine in a N_2 atmosphere. Compared with undoped pyrolyzed β -CD, N-doping led to a 30.3-fold enhancement in the pseudo-first-order rate constant for catalytic ozonation of oxalic acid (OA), and complete degradation of 50 mg/L OA was achieved in 45 min. Apart from the specific surface area boosting from 78.9 to 16.2 m^2/g after N doping, the OA degradation results and material characterization also suggested that quaternary N was the main active site, which was further validated by density functional theory (DFT) simulations. DFT simulations also suggested that C atoms with high charge densities adjacent to N dopants exhibited considerable potential for the catalytic dissociation of ozone. Electron paramagnetic resonance (EPR), radical quenching, and in situ Raman studies indicated occurrence of surface oxidation pathway apart from the radical-based one. Ozone on the catalyst surface was decomposed into surface-adsorbed atomic oxygen (${}^*O_{ad}$) and free peroxide (*O_2 free). Both ${}^*O_{ad}$ and *OH , which was further evolved on the surface or in bulk solution, contributed to OA destruction. These insights into the catalytic ozonation mechanism on N-doped nanocarbons will advance their practical application to the catalytic degradation of organic pollutants.

1. Introduction

Catalytic ozonation has emerged as one of the prevailing AOP technologies for the high-efficiency destruction of persistent organic pollutants (POPs) [1–3]. In addition to ozone molecules, which have a high affinity for attacking the unsaturated bonds in POPs, the generated reactive oxygen species (ROS) such as hydroxyl radical (*OH) and superoxide radical anion (O_2^-) also obtain high redox potentials, which are critical for decomposing intermediates and achieving complete mineralization to inorganic forms [4,5]. Owing to surface Lewis acidic sites and variable valence states that facilitate ozone adsorption and accelerate electron transfer, metal-based materials, especially transition metal oxides, are highly reactive for ozone activation [6–9]. Nevertheless, on exposure to ozone and the produced ROS, leaching from metal catalysts is unavoidable, which unfortunately results in

secondary pollution.

Metal-free catalysts, especially nanocarbons, have emerged as sustainable alternatives to metal-based catalysts owing to their high catalytic activities resulting from their unique electronic and chemical properties as well as their nanoscale structural features [10–12]. Using nanocarbons, excellent outcomes have been achieved in energy conversion, electrochemical applications, and environmental remediation [13–16]. In pioneering studies, we discovered the excellent catalytic ozonation activity of reduced graphene oxide (rGO) for the mineralization of aqueous organic pollutants [17,18]. Both experimental results and theoretical calculations have indicated that surface defect sites and oxygen functionalities are catalytically reactive. Moreover, heteroatom doping can further enhance the catalytic activity of nanocarbons [19]. Owing to difference in electronegativity, the incorporation of heteroatoms such as N, P, and B into the carbon framework

* Corresponding authors.

E-mail addresses: ybxie@ipe.ac.cn (Y. Xie), songwy@cup.edu.cn (W. Song).

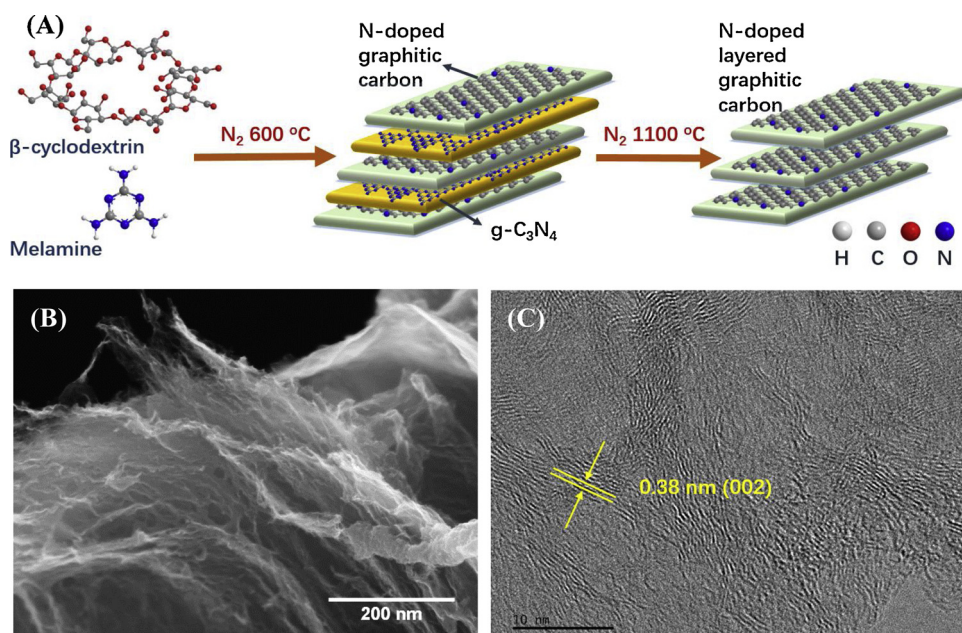


Fig. 1. (A) Synthesis route for N-doped nanocarbons. (B) SEM and (C) HRTEM images of N3C-1100.

results in redistribution of the charge density and allows tailoring of the band structure of sp^2 carbons [20–22]. In a very recent study, we reported a remarkable improvement in catalytic activity by doping N atoms in rGO using a facile microwave reduction method, and quaternary N was suggested to play a pivotal role [23]. However, the understanding of the catalytic improvement resulting from heteroatoms doping remains insufficient. Previous studies only reported physiochemical properties variations after heteroatoms doping and correlated with the enhancement in catalytic activities, yet the carbon matrix charge density variation brought by heteroatom doping and adsorption behavior of ozone molecules on the doping sites are obscure. Moreover, the synthesis routes for these nanocarbons are usually cost-intensive, requiring complicated procedures under harsh conditions with low yields. Thus, it is important to seek facile and cost-efficient methods for synthesizing reactive nanocarbons in high yields.

Hydroxyl radical ($\cdot\text{OH}$)-based reactions have been recognized as the dominant pathway for the destruction of the organic pollutants in most catalytic ozonation processes. However, some recent studies have revealed the possibility of degradation pathways that do not rely on $\cdot\text{OH}$ [2,24]. A few studies have demonstrated the existence of a non-radical pathway for the direct destruction of pollutants at the surface of the catalyst [25–28]. Bing et al. reported a direct surface oxidation pathway for pharmaceuticals involving surface-active oxygen and peroxide complexes produced by the dissociation of ozone molecules utilizing mesoporous $\text{Ti-Al}_2\text{O}_3$ as a catalyst [25]. Similar observations were also reported by Zhang et al for catalytic ozonation with ceria supported copper oxide [26]. Meanwhile, the decoration of the graphitic carbon lattice with nitrogen dopants has also been reported to alter the reaction mechanism owing to the high electronegativity resulting from substitutional N-doping [29–31]. Therefore, the organic pollutant degradation pathway during catalytic ozonation over N-doped nanocarbons requires elucidation.

Herein, we developed a facile one-step pyrolysis method for synthesizing N-doped graphitic nanocarbons. In this approach, β -cyclodextrin (β -CD), which has a cyclic truncated cone shape, was chosen as the carbon precursor to prepare a layered graphitic structure [32]. Melamine, which can bind to the hydrophobic central cavity of β -CD through hydrogen bonding, was used as the nitrogen precursor. Through a sectional heating profile (25–600–1100 °C), layered N-doped graphitic nanocarbons was produced in a N_2 atmosphere. Compared

with undoped pyrolyzed β -CD, N-doping led to a significant enhancement of the catalytic ozonation activity. Moreover, the effects of the pyrolysis temperature and N-doping level on the catalytic activity were investigated. Density functional theory (DFT) simulations were performed to provide in-depth insights into the active N species involved in the catalytic oxidation process. In addition to $\cdot\text{OH}$ oxidation in bulk solution, surface oxidation of oxalic acid (OA) by O_3 dissociation intermediates was revealed by both quenching studies and electron paramagnetic resonance (EPR) measurements. This study not only provides a facile protocol for the scalable synthesis of surface-engineered nanocarbons, but also reveals the effect of N-doping on the catalytic ozonation mechanism.

2. Experimental

2.1. Chemicals and materials

Melamine (99.5%), β -CD (98.0%), *tert*-butanol (t-BA, 99.0%), OA (99.9%), *para*-hydroxybenzoic acid (pHBA, 99.9%), *para*-chlorobenzoic acid (pCBA, 99.8%), and 4-nitrophenol (4-NP, 99.9%) were procured from Aladdin Biochemical Reagent Co., Ltd. Commercial graphite (99.99%) was purchased from Alfa Aesar. Potassium permanganate (99.5%), sulfuric acid (98%), hydrochloric acid (37%), ammonium nitrate (99.5%), and hydrogen peroxide (H_2O_2 , 30%) were obtained from Beijing Chemical Plant. Sodium azide (NaN_3 , 99.0%) was obtained from Fuchen Chemical Reagent Co., Ltd. 5,5-Dimethyl-1-pyrroline (DMPO) and 2,2,6,6-tetramethyl-4-piperidone (TEMP) were purchased from Sigma-Aldrich. All the chemicals were utilized without further purification.

2.2. Preparation of catalysts

In a typical synthesis, 1 g of β -CD and 3 g of melamine were dispersed into a mixture of methanol (50 mL) and ultrapure water (50 mL) and stirred overnight at 70 °C on a hotplate. Then, the obtained solid mixture was heated to 600 °C in N_2 with a ramping rate of 2 °C/min. After heating for 4 h, the temperature was further raised to 1100 °C with the same ramping rate and maintained for another 3 h. After grinding, the obtained product was denoted as N3C-1100. N1C-1100 and N4C-1100 were also prepared by the same procedure using a 1:1

mass ratio of β -CD and melamine and a 1:4 mass ratio of β -CD and melamine, respectively. Meanwhile, samples with a 1:3 mass ratio of β -CD and melamine were also prepared with final pyrolysis temperatures of 600 and 800 °C (denoted as N3C-600 and N3C-800, respectively). A schematic of this synthesis route is shown in Fig. 1A. For comparison, β -CD pyrolyzed using the same heating profile in the absence of melamine was denoted as CD-1100. In addition, this N-doping protocol was applied to GO and chitosan to synthesize N-RGO and N-CHI, respectively. And the corresponding undoped samples were also prepared and denoted as RGO and CHI, respectively. The detailed synthesis procedures are described in Text S1 in the supplementary data (SD).

2.3. Characterization methods

The as-prepared catalysts were investigated using field emission scanning electron microscopy (FESEM; ZEISS GeminiSEM 300), transmission electron microscopy (TEM; JEOL 2100F (UHR)), X-ray diffraction (XRD; PANalytical X'Pert-PRO MPD), N_2 sorption isotherms (Micrometrics Tristar 3000), thermogravimetric analysis (TGA; Mettler Toledo STAR^e), X-ray photoelectron spectroscopy (XPS; Thermo Fisher Scientific ESCALAB 50Xi), Raman spectroscopy (Renishaw Invia Reflect), and EPR (Bruker EMX). Text S2 in the SD provides detailed descriptions of the characterization methods.

2.4. Evaluation of catalytic performance

Ozonation/catalytic ozonation experiments were performed in a 0.5 L semi-batch glass reactor at 25 °C. Ozone generated from high-purity oxygen (99.9%) was bubbled into the bottom of the reactor via a glassy porous diffusor, and the concentration of gaseous ozone was monitored using an online ozone detector (Ansers Ozomat GM). The inlet flow rate of ozone was set as 100 mL/min using a mass flowmeter. In a typical test, 0.05 g of catalyst was added to the reaction solution. The mixed solution was allowed to stir for 15 min to reach adsorption–desorption equilibrium. Samples were withdrawn from the reactor and filtered through a 0.22 μ m PTFE filter under the certain time intervals. The filtrate was then purged with a N_2 flow. An ultra-high-performance liquid chromatography system (Thermo Fisher Scientific U3000 series) equipped with an RSLC column was used to analyze the concentration of organic pollutants in the withdrawn samples. The flow rate was 0.25 mL/min and the mobile phases were mixtures of diluted phosphate acid solution (2 mM) and methanol with proportions of 80% vs. 20% for OA analysis, 60% vs. 40% for pHBA and PCBA analysis, and 30% vs. 70% for 4-NP analysis. To determine the mineralization rate of the target pollutants, the total organic carbon (TOC) was determined using a Shimadzu TOC-VCPh analyzer. To evaluate the stability of the catalyst over multiple runs, the catalyst was recycled after each test by vacuum filtration, then washed with ultra-pure water three times, and dried at 80 °C overnight.

2.5. Theoretical calculations

To investigate the chemisorption of ozone onto different graphene models, DFT calculations were performed with the Vienna Ab initio Simulation Package (VASP) using the Perdew–Burke–Ernzerhof (PBE) functional for the exchange correlation energy with a semiempirical van der Waals (vdW) correction to account for dispersion interactions. Text S3 in the SD provides a detailed description of the DFT calculations.

3. Results and discussion

3.1. Effect of N-doping on physicochemical properties

Pyrolysis of β -CD in a N_2 atmosphere resulted in the formation of an irregular bulk structure with a smooth surface and curled edges (Fig.

S1A). The presence of melamine as a N precursor dramatically altered the surface morphology of the as-prepared carbonaceous materials. As illustrated in Fig. 1B, a wrinkled surface with exfoliated edges was observed for N3C-1100. Melamine was transformed into C_3N_4 in the low-temperature range (< 600 °C), and the formed C_3N_4 layers intertwined with the carbonized layered cyclodextrin to generate an intercalated structure. Meanwhile, a minor amount of melamine was incorporated within the carbonized cyclodextrin structure to form N dopants [22]. During the prolonged heating process (600 °C for 4 h), sublimation of the intercalated C_3N_4 occurred owing to its structural instability, leaving only the structurally doped N. Further elevation of the pyrolysis temperature to 1100 °C consolidated the N dopants and developed a graphitic lattice. Removal of intercalated C_3N_4 from within the composite structure not only caused the wrinkled surface, but also resulted in porous and layered edges, which are similar to those in exfoliated rGO derived from the vaporization of the oxygen functionalities of GO [18]. Moreover, the high annealing temperature (1100 °C) applied could cause the decomposition of N-dopants and collapse of carbon framework, leading to formation of a more porous structure. As summarized in Table S1, owing to its wrinkled surface and porous layered edges, N3C-1100 had a larger specific surface area (SSA, 78.9 vs. 16.2 m^2/g) and pore volume than CD-1100 (0.13 vs. 0.01 cm^3/g). Furthermore, as illustrated by the TGA/DSC curves in Fig. S3A, only one exothermal peak was observed, centered at 675 °C, which was assigned to the collapse of the carbon skeleton [33]. The absence of an endothermic peak at approximately 600 °C confirmed that most of C_3N_4 was sublimated during the pyrolysis process [34]. Increasing the N to C precursor ratio led to the formation of more intercalated C_3N_4 , and sublimation resulted in a higher SSA and pore volume (Fig. S2 and Table S1). The SSA of N3C-1100 ($78.9\text{ m}^2/\text{g}$) was 2.6-fold greater than that of N1C-1100 ($29.6\text{ m}^2/\text{g}$).

The incorporation of N dopants also enhanced the graphitic level within the carbonaceous materials. For CD-1100, the disordered graphitic lattice observed in the HRTEM image (Fig. S1C) revealed the undeveloped nature of the graphitic structure. However, in N3C-1100, an ordered graphitic lattice was developed (Fig. 1C), confirming the contribution of melamine to the formation of the graphitic phase. N3C-1100 exhibits a larger (002) interlayer spacing than pristine graphite (0.38 vs. 0.34 nm), indicating the integration of N atoms within the graphitic lattice [35]. The substitutional N atoms also break the internal strain balance of the original carbon network, which induces layer curvature [36,37]. In the XRD patterns (Fig. S5), the peak intensity of the (002) planes for N3C-1100 was notably higher than that of CD-1100. Furthermore, the absence of the characteristic peak at 13.1° for the (001) plane suggests the successful sublimation of C_3N_4 [34].

3.2. Catalytic ozonation activities of undoped/N-doped catalysts

OA, which is quite recalcitrant to ozone attack ($k_{O_3} = 0.04\text{ M}^{-1}\text{ s}^{-1}$), was used herein as a target pollutant to evaluate the catalytic performance of the as-synthesized carbocatalysts [17]. As expected, less than 10% of OA was destroyed by single ozonation (Fig. S6). Meanwhile, trivial adsorption (~5%) was observed for these catalysts, indicating a weak interaction between the OA molecules and the carbon surface at pH 3.2. CD-1100 with a lower SSA has a better performance on adsorption than N3C-1000. It should be noted that the surface charge of the catalyst within the solution is another critical factor affecting the electrostatic force between the catalyst surface and the target pollutant. With a pH_{pzc} of 3.7 according to the zeta potential plot, N3C-1100 was slightly protonated in ambient solution with pH 3.2. CD-1100 obtained a pH_{pzc} of 3.1, and thus the surface was more positively charged than N3C-1100. While OA molecules with a pK_a of 1.47 were negatively charged at pH 3.2. Therefore, the more positively charged surface of CD-1100 resulted in a higher adsorption ability than N3C-1100.

For catalytic ozonation using CD-1100 as the catalyst, only 18% of

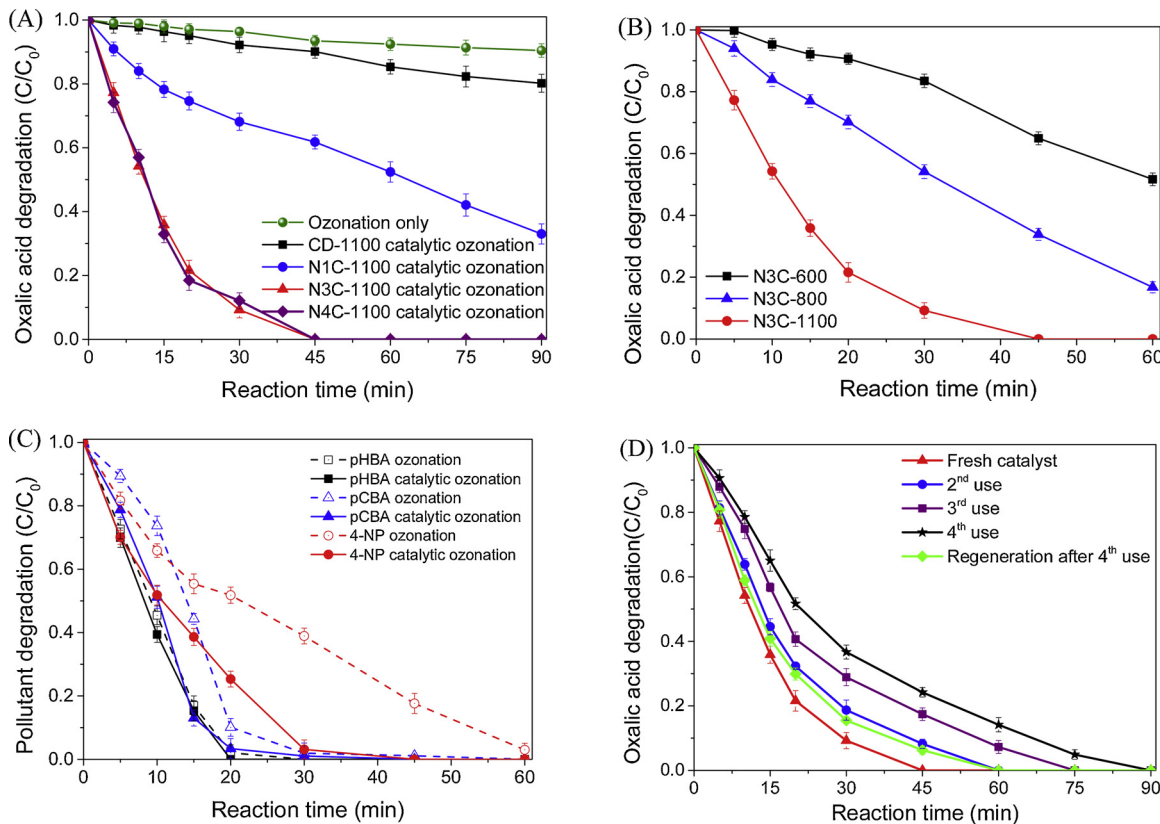


Fig. 2. (A) OA removal with different catalysts; (B) Effect of pyrolysis temperature on catalytic activity; (C) Degradation of various pollutants by N3C-1100 catalytic ozonation; and (D) Catalytic stability and re-generation tests of N3C-1100 for OA removal. Catalyst loading: 0.1 g/L; $[OA]_0$: 50 mg/L; $[pHBA]_0$: 50 mg/L; $[pCBA]_0$: 50 mg/L; $[4\text{-NP}]_0$: 50 mg/L; ozone flow rate: 100 mL/min; ozone concentration: 25 mg/L; temperature: 25 °C; initial pH: 3.2 (adjusted by adding 0.01 M HCl/NaOH to the solution).

OA was degraded after 1 h. N-doping could significantly enhance the catalytic activity. N1C-1100 obtained a greater catalytic activity than the undoped CD-1100, resulted in 70% of OA removal after 90 min. For N3C-1100, complete OA removal was achieved within 45 min. Further increase the melamine/ β -CD mass ratio did not result in an obvious improvement in catalytic activity, and N4C-1100 possessed a similar catalytic activity to N3C-1100 (Fig. 2A). The as-calculated pseudo-first-order reaction rate constant for N3C-1100 was 30.3-fold greater than that for undoped CD-1100, and also higher than that for N-RGO (Table S1 and Fig. S8C). Moreover, compared with N-RGO, N3C-1100 displayed robust structural stability against ozone and ROS attack (Fig. S9). Furthermore, the effect of the annealing temperature on the activity of the N-doped catalysts was investigated (Fig. 2B). Increasing the annealing temperature enhanced the catalytic ozonation activity. N3C-600 exhibited inferior activity to N3C-1000, with catalytic ozonation removing only 50% of OA after 60 min. Fig. 2C displays the oxidation abilities of the N3C-1100/O₃ system towards various organic pollutants (pCBA, 4-NP, and pHBA). The variation in the degradation efficiencies suggests that the generated ROS have higher affinities for electron-withdrawing groups (−Cl, −NO₂) with highly delocalized electron densities than for electron-donating groups (−OH) with nucleophilic properties. The corresponding TOC removal profiles exhibit a similar trend (Fig. S10B). The effect of the solution pH on 4-NP and the corresponding TOC removal profiles with the N3C-1100/O₃ system are depicted in Fig. S11. Variation of solution pH exerted somewhat influence on 4-NP removal by affecting the ROS generation and surface charge of the catalyst.

Various factors contributed to N3C-1100 having a higher catalytic activity of than the other as-synthesized materials. The greater SSA of N3C-1100 not only facilitated the adsorption of OA molecules but also caused more edge structures to be exposed, which contributed to the

higher catalytic activity. Our previous study revealed that the armchair and zigzag edges of graphitic carbon rings exhibit high activities for ozone self-decomposition to produce ROS [17]. Considering the dramatic increase in the catalytic activity after N-doping, other more critical factors could affect the catalytic activity. Previous studies revealed that defect sites played a critical role in carbocatalysis, as delocalized electrons and carbon dangling bonds may provide high chemical potentials [22,38]. Raman spectra were employed to evaluate the defect levels in the as-prepared carbonaceous materials (Fig. 3A). Compared with CD-1100, the N-doped catalysts exhibited a slightly higher I_D/I_G owing to the exposure of more edge defects. Although similar defective levels were observed for N3C-600, N3C-800, and N3C-1100, the slightly higher I_D/I_G of N3C-600 did not result in the best catalytic activity, which could be ascribed to the redistribution of charge density caused by N-doping or the existence of other more effective active sites.

Doping sites are often regarded to be catalytically active because N-doping can stimulate electron transfer from adjacent C atoms owing to the higher electronegativity of N [20,37,39]. Cryo-EPR at −183 °C (Fig. 3B) was utilized to investigate the N-doping level by detecting the signals of the unpaired electrons and spins of the doped N atoms [40,41]. CD-1100 was EPR silent owing to the absence of unpaired electrons. For both N1C-1100 and N3C-1100, sharp EPR signals with a Landé factor of $g = 2.0047$ were observed owing to the introduction of N atoms. In addition, the higher N-doping level gave rise to a larger number of unpaired electrons and spins, thus resulting in a higher intensity of the EPR signal [42]. To quantify the N-doping level and differentiate the doped N species, the surface compositions of the as-prepared catalysts were examined by XPS. Based on the full elemental surveys (Fig. S12 and Table S2), N3C-600 contained the highest amount of nitrogen owing to the presence of unsublimated C₃N₄, as confirmed by TGA (Fig. S3), but exhibited the poorest activity. N3C-800 and N3C-

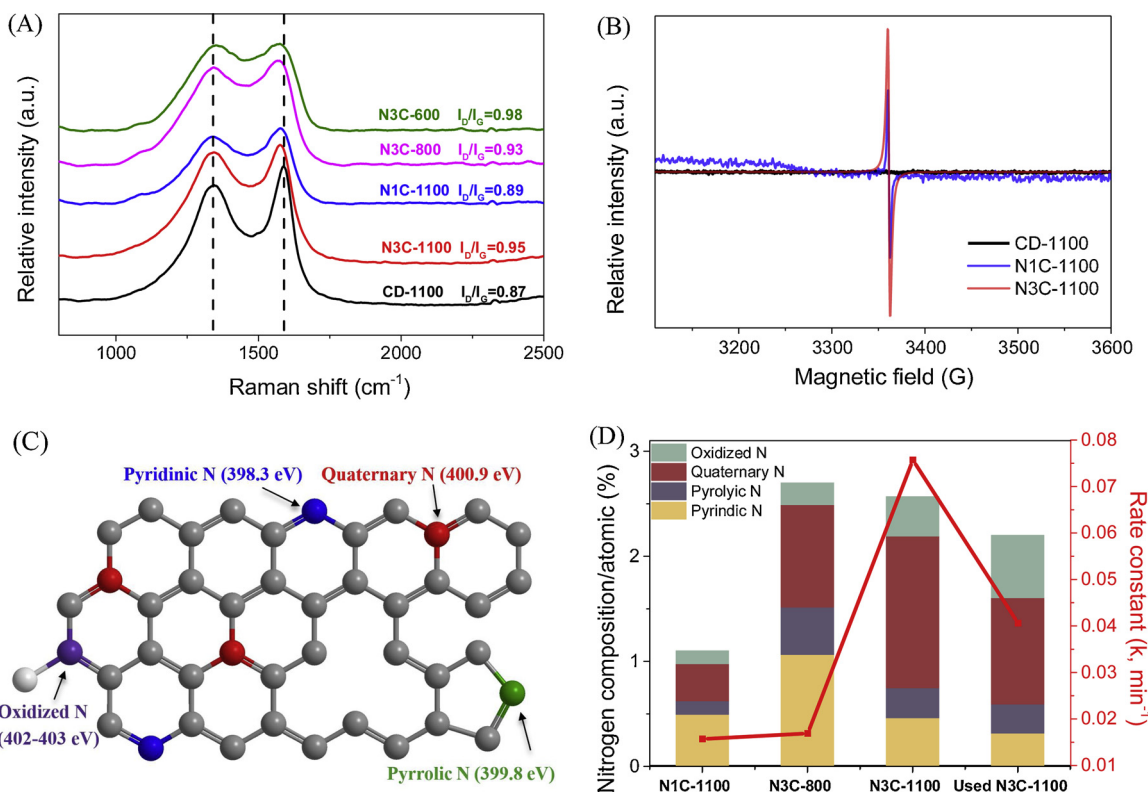


Fig. 3. (A) Raman spectra of the as-prepared carbonaceous materials; (B) Cryo-EPR spectra of the nanocarbons; (C) Schematic of N dopants in a graphene lattice; and (D) N species composition vs. pseudo-first-order reaction rate. EPR operating conditions: temperature: -183°C (90 K); centerfield: 3360 G; sweep width: 500 G; microwave frequency: 9.057 GHz; modulation frequency: 100 GHz; power: 10.00 mW.

1100 possessed similar surface amounts of N, but their catalytic activities differed notably.

The types of doped N species play a pivotal role in determining the catalytic activity. To differentiate the N species, the N1s XPS spectra (Fig. S13) of the N-doped nanocarbons were deconvoluted into four components centered at 398.3, 399.8, 400.9, and 402.9 eV, which corresponded to pyridinic N, pyrrolic N, quaternary N, and oxidized N, respectively [43,44]. A schematic illustration of the N dopants within a graphene lattice is shown in Fig. 3C. The substituted N atoms tailor the electrical properties of the sp^2 -hybridized carbon lattice via conjugation between the lone-pair electrons of the doped N atoms and the homogeneous π -system [21]. Observed from the N species distinguished for N3C-600 (Table S2), pyridinic N was the dominant N species at low pyrolysis temperatures. Owing to the higher thermal stability of quaternary N, elevating the annealing temperature from 600 to 1100°C led to an increase of quaternary N from 10% to 59%. Thus, quaternary N was the dominant N species at high pyrolysis temperatures. Based on the plot of the composition of N species against the pseudo-first-order reaction rate in Fig. 3D, an increase in the quaternary N content enhanced the catalytic OA degradation reaction rate. Previous studies also suggested that quaternary N plays a crucial role in catalytic activity enhancement in carbocatalysis [22]. To further illustrate the catalytic activity enhancement resulting from quaternary N, the turnover frequency (TOF) of the catalysts was estimated based on the OA degradation efficiency and their BET surface areas. The details of the TOF calculation are described in Text S4 in the SD. The TOFs for N3C-600, N3C-800, and N3C-1100 were calculated to be 4.4×10^{-4} , 1.4×10^{-3} , and $1.9 \times 10^{-3} \text{ s}^{-1} \text{ m}^{-2}$, respectively. Thus, a higher quaternary N content promoted the catalytic activity and corresponding TOF for OA removal.

The reusability of N3C-1100 was evaluated using a four-run catalytic ozonation test (Fig. 2D). The used catalyst was ultrasonicated for 20 min after each recycle and then washed with ultrapure water for 3

times. Slight passivation of the catalyst occurred after multiple cycles. Complete OA removal was achieved in 45 min with fresh catalyst, however, this became 90% in the 2nd cycle, and it further reduced to 76% in the 4th cycle. Deactivation has often been attributed to changes in the physicochemical properties of the catalyst surface as well as agglomeration. Comparing with the fresh N3C-1100, slight changes were observed on the surface area and pore volume of the used catalyst. This suggested deactivation would occur by blockage of the active sites or physical changes of the catalyst surface. We then evaluated the effect of the low-temperature annealing on the stability recovery. The catalyst after the 4th use was annealed in air at 250°C for 3 h to remove potential adsorbed degradation intermediates. It was found that the activity of the catalyst was greatly recovered and complete OA removal could be achieved in 60 min. XPS survey suggested that the oxygen content of the regenerated catalyst was slightly reduced (Fig. S12 and Table S2), which could be probably ascribed to the removal of the adsorbed degradation intermediates. Correspondingly, both of the surface area and pore volume of the regenerated catalyst increased slightly (Table S1), and some of the mesopores were also restored (Fig. S14). Changes in the surface chemistry of N3C-1100 might also play a key role in this passivation process. XPS analysis revealed that the N dopants on the surface of N3C-1100 decreased by 10% after the 4th cycle, which might cause by breakage of C–N bonds by attack of ozone and highly reactive ROS. This decrease in the N-doping level would reduce the number of active sites. In addition, extended exposure to the catalytic ozonation environment also resulted in the oxidation of reactive quaternary N. Compared with the fresh catalyst, the oxidized N was increased from 12.3% to 14.3%. It is worth noting that the low-temperature treatment would lead to a negligible influence on the doped N and its composition (Table S2).

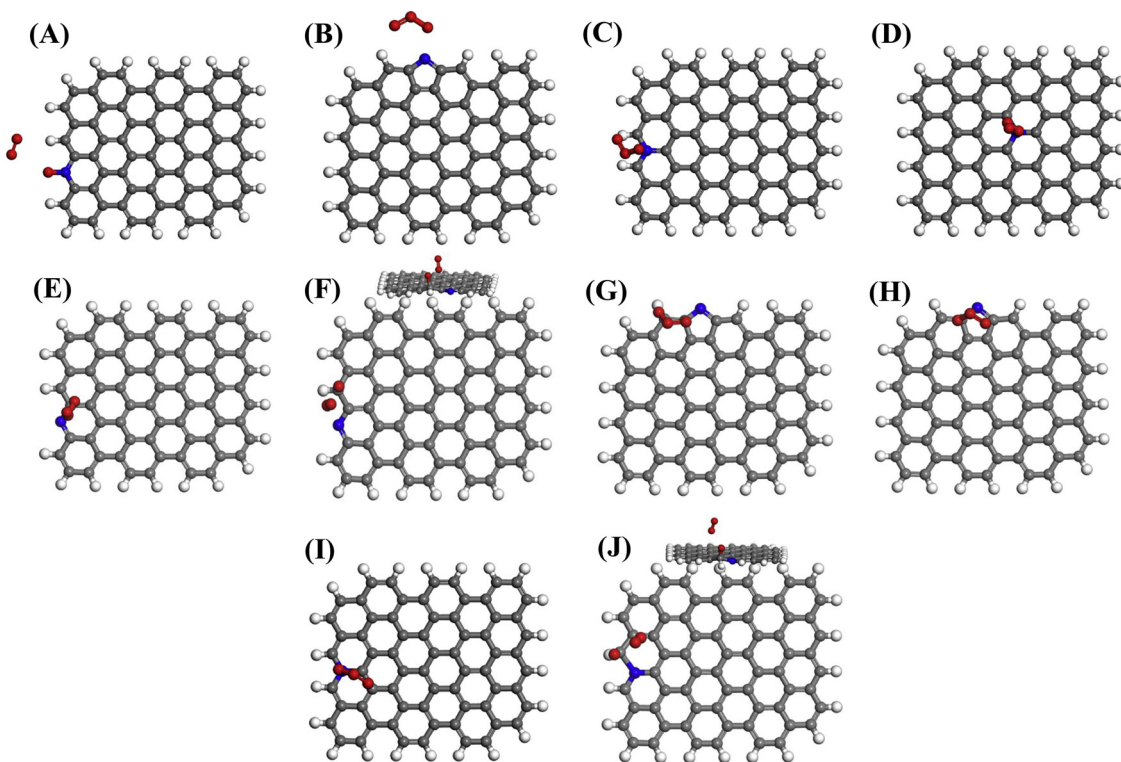


Fig. 4. (A–D): DFT models of the favorable adsorption structures for an ozone molecule on different N-doping sites in a graphene layer: (A) Pyridinic N, (B) Pyrrolic N, (C) Edge quaternary N, and (D) In-frame quaternary N. (E–J): DFT models of the favorable adsorption structures for an ozone molecule on C atoms adjacent to the different N-doping sites in a graphene layer: (E) C1 atom of pyridinic N, (F) C2 atom of pyridinic N, (G) C1 atom of pyrrolic N, (H) C2 atom of pyrrolic N, (I) C1 atom of edge quaternary N, and (J) C2 atom of edge quaternary N. Color scheme: Grey: C; blue: N; white: H; red: O (For interpretation of the references to colour in this figure legend, the reader is referred to the web version of this article).

3.3. Unveiling the active sites using DFT simulations

To simplify the DFT simulations, single-layer graphene models were constructed with different N-doping species (pyridinic N, pyrrolic N, and quaternary N) on the edge and in-frame quaternary N (Fig. S15). Situating an O_3 molecule near the pyridinic N gave rise to its spontaneous dissociation with an adsorption energy of -1.32 eV (Fig. 4A and Table S3). The O_3 molecule dissociated into a surface-bound atomic oxygen ($^*\text{O}_{\text{ad}}$) through the formation of a weak C–O bond with the graphene matrix and a free peroxide ($^*\text{O}_2 \text{ free}$). However, the lower degree of defects and smaller SSA of N3C-800 and N1C-1100 might result in decreased exposure to pyridinic N, resulting in the inferior catalytic activities of these nanocarbons, as pyridinic N only exists at structural defects and on the edges along the graphene boundaries. As demonstrated in Table S3, edge quaternary N has a superior catalytic activity to in-frame quaternary N and pyrrolic N in terms of both the length of O–O bond within ozone molecule ($\text{l}_{\text{O–O}}$) and adsorption energy. Compared with that in pristine ozone (1.285 \AA), $\text{l}_{\text{O–O}}$ was stretched to 1.405 , 1.321 , and 1.297 \AA in the final adsorption state for edge quaternary N, in-frame quaternary N, and pyrrolic N, respectively. The corresponding adsorption energies were -0.74 , -0.58 , and -0.24 eV , respectively.

Our DFT simulation revealed that N-doping also altered the charge distribution of the C atoms adjacent to the N-doping sites (Fig. S17). To evaluate the effect on ozone dissociation, DFT simulations were performed by situating O_3 on adjacent C sites with a sparse charge density (C1) and a dense density (C2). Detailed C1 and C2 atom labeling for the different models is illustrated in Fig. S17. The simulation results suggested that a higher charge density favored ozone dissociation. For both the pyridinic N and quaternary N models, the C2 atoms with a concentrated charge density resulted in the catalytic dissociation of O_3 into $^*\text{O}_{\text{ad}}$ and $^*\text{O}_2 \text{ free}$. The sparse charge density of the C1 atoms only

resulted in a slight stretch of $\text{l}_{\text{O–O}}$ with a low adsorption energy. Notably, the C2 atom in the quaternary N model was quite active for ozone adsorption, with a strong adsorption energy of -1.9 eV (Fig. 4J), which is higher than that of pyridinic N and its adjacent C atoms. Therefore, the adjacent C atoms with a dense charge density from quaternary N played a pivotal role in promoting the catalytic activity. A different situation was observed for the C atoms next to pyrrolic N. Although doping with pyrrolic N altered the electron distribution and enabled the edge structures to obtain more electron charge (Fig. 4G and H), the five-membered ring hindered the electron transfer process, thus impeding ozone adsorption. Thus, this study revealed that in addition to the N-doping sites, the adjacent C atoms in six-membered rings with concentrated charge density zones, especially the C atoms connected to quaternary N, are potential active sites for catalytic ozone dissociation.

3.4. Mechanistic insights into ROS generation

Quenching tests were performed utilizing OA as the target pollutant (Fig. 5A). Our previous study suggested that $\cdot\text{OH}$ was the dominant ROS for catalytic ozonation of an aliphatic acid [18]. t-BA, which has a rapid reaction rate towards $\cdot\text{OH}$ ($k_{\cdot\text{OH}} = (3.8 - 7.6) \times 10^9 \text{ M}^{-1} \text{ s}^{-1}$) but a low reaction rate with ozone molecules ($k_{\text{O}_3} = 3 \times 10^{-5} \text{ M}^{-1} \text{ s}^{-1}$), was employed as the $\cdot\text{OH}$ quenching agent [45]. The addition of 12 mM t-BA (t-BA/ O_3 = 4, molar ratio) successfully quenched the catalytic ozonation process. Only 70% of OA was degraded after 60 min. To exclude the influence of other ROS, NaN_3 was employed as an inorganic quenching agent for $^1\text{O}_2$ [5,18]. Since azide anions react with O_3 in neutral or alkaline solutions, the solution pH was adjusted to 3.2 after the addition of NaN_3 to inhibit this reaction [46,47]. Azide anions also exhibit comparable reaction rate constants for $^1\text{O}_2$ and $\cdot\text{OH}$ ($2 \times 10^9 \text{ M}^{-1} \text{ s}^{-1}$ vs. $1.2 \times 10^9 \text{ M}^{-1} \text{ s}^{-1}$) [48,49]. However, the observation of similar OA degradation profiles in the presence of NaN_3

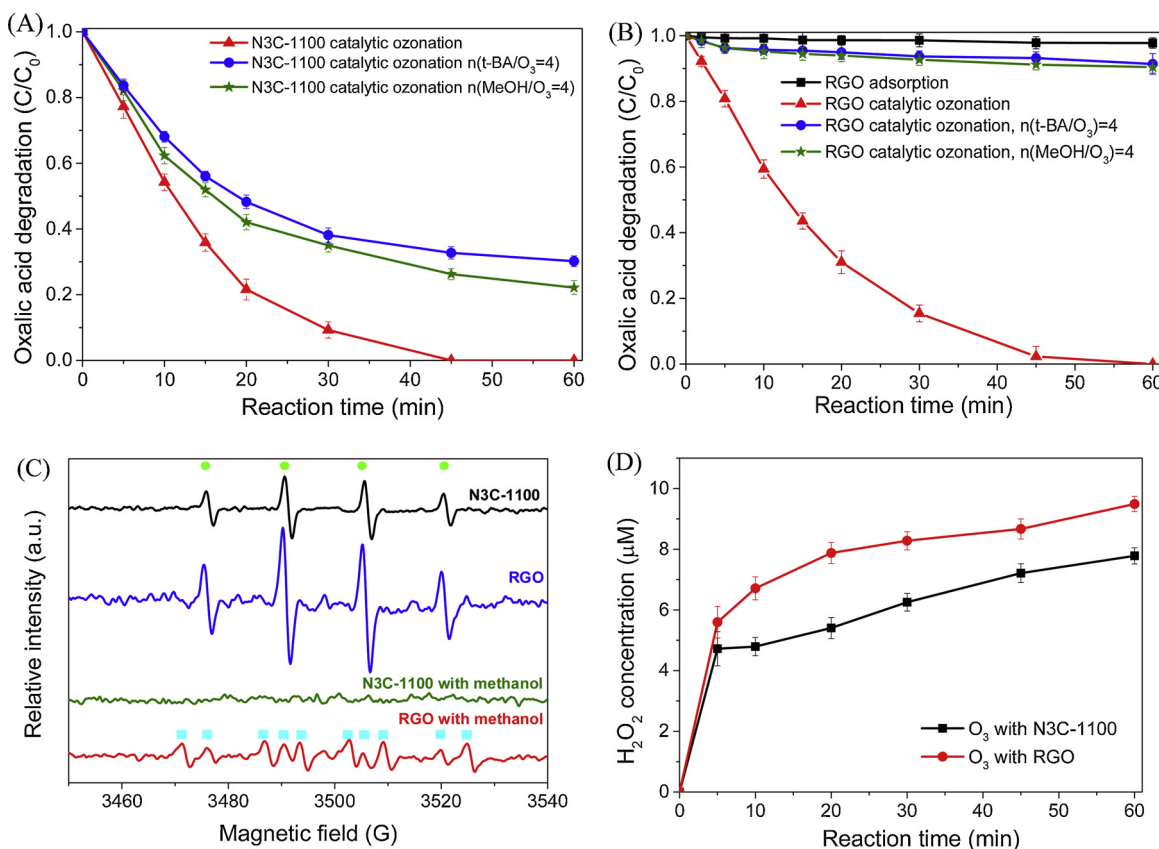


Fig. 5. Radical quenching during (A) N3C-1100 catalytic ozonation and (B) RGO catalytic ozonation; (C) EPR spectra with DMPO as a spin trapping agent; and (D) variation in the H₂O₂ concentration for N3C-1100. Catalyst loading: 0.1 g/L; [OA]₀: 50 mg/L; ozone flow rate: 100 mL/min; ozone concentration: 25 mg/L; temperature: 25 °C; initial pH: 3.2 (adjusted by adding 0.01 M HCl/NaOH solution). EPR operating conditions: centerfield: 3490 G; sweep width: 100 G; microwave frequency: 9.057 GHz; modulation frequency: 100 GHz; power: 18.3 mW.

and t-BA revealed that the contribution of $^1\text{O}_2$ to OA degradation was negligible (Fig. S18).

The effect of the t-BA dosage on the quenching effect was evaluated to further probe the reaction pathway. Increasing the t-BA/O₃ ratio did not result in a further quenching effect (Fig. S19). Methanol, which can scavenge both free and adsorbed ·OH with a fast reaction rate ($k_{\cdot\text{OH}} = 9.7 \times 10^8 \text{ M}^{-1} \text{ s}^{-1}$), was also utilized to examine the contribution of ·OH [50,51]. The addition of 12 mM methanol (methanol/O₃ = 4, molar ratio) produced a similar quenching effect to that of t-BA (Fig. 5A). Moreover, increasing the methanol dosage (1000:1, molar ratio) only gave rise to a minor enhancement (Fig. S19). For comparison, radical quenching tests were also performed with as-synthesized RGO under the same experimental conditions (Fig. 5B). Significant quenching effects were observed in both the t-BA and methanol quenching tests, suggesting that OA degradation involved a ·OH radical oxidation pathway during RGO catalytic ozonation. For N3C-1100, the partial inhibition observed after the addition of alcohols indicated that the N-doped nanocarbons could possibly induce another type of reaction pathway apart from the ·OH-based one.

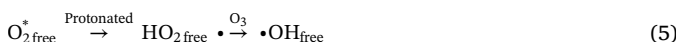
EPR spectra were then collected to investigate the variations in ROS during catalytic ozonation with N3C-1100 and RGO as catalysts (Fig. 5C). The EPR spectra of N3C-1100 and RGO both exhibited the characteristic peaks of DMPO-OH adducts (hyperfine splitting couplings of $a_N = a_H = 14.9 \text{ G}$), suggesting the production of ·OH. However, the signal intensities of the DMPO-·OH adducts with N3C-1100 were lower than those with RGO, indicating that less ·OH was generated. Methanol was then added to the reaction solution to quench ·OH generated during the EPR tests. DMPO-·OOH adduct signals with hyperfine splitting constants of $a_N = 14.2 \text{ G}$, $a_H^\beta = 11.4 \text{ G}$, and $a_H^\gamma = 1.2 \text{ G}$ were observed when RGO was employed as the catalyst, indicating the

generation of HO₂[·]/O₂^{·-}, which act as a bridge to accelerate the formation of ·OH [52]. However, with N3C-1100, insignificant signals were detected in the presence of methanol, suggesting that ·OH was the dominant generated radical.

In catalytic ozonation, a surface oxidation process that relies on the ozone dissociation products has been suggested as another reaction pathway for pollutant destruction [24,26,27]. Moreover, owing to the redistributed of electron charges near N-doping sites, N-doping facilitates the attachment of oxidants to form surface-oxidant complexes for the destruction of adsorbed organics [22,31,53,54]. To investigate the ozone dissociation products on the N3C-1100 surface, in situ Raman spectroscopy was employed (excitation wavelength: 532 nm). As illustrated in Fig. S20, a new band emerged at 924 cm⁻¹ on the catalyst surface in the presence of an ozone flow, which was assigned to *O_{ad} [55]. With a high oxidation potential of 2.43 V, *O_{ad} could directly destroy OA molecules [25]. Previous studies also reported the existence of *O_{2 ad} based on the observation of a band between 880 and 892 cm⁻¹ and ascribed the production of these surface-bound intermediates to the surface hydroxyl groups on metal-based catalysts [6,25,56]. However, in this study, the characteristic peak of *O_{2 ad} was not observed. Our DFT simulations indicated that O₃ would dissociate into a surface-bound atomic oxygen (*O_{ad}) and free peroxide (*O_{2 free}) on the active sites of the N3C-1100 surface. Therefore, N-doping may alter the reaction mechanism and facilitate the generation of *O_{2 free}.

In the catalytic ozonation of aliphatic acids, the major route for H₂O₂ formation arises from the chain termination reaction of HO₂[·]/O₂^{·-} and ·OH in acidic solution [2,57]. Fig. 5D displays the generation of H₂O₂, as measured using the horseradish peroxidase method [58]. A lower amount of H₂O₂ was generated during the N3C-1100 catalyzed ozonation reaction than during the RGO catalyzed reaction, suggesting

that less HO₂[·]/O₂^{·-} and ·OH were produced, which is in accordance with the EPR results. Meanwhile, the O₃ concentration in the outlet stream ([O₃]_{out}) was monitored during OA degradation (Fig. S21), and ozone consumption rate can be calculated by Eq. S4 in SD. In ozonation, the ozone consumption rate reached 20% at 5 min, and then quickly decreased to a rather low range, suggesting ozone was merely consumed ozone after getting saturated in the solution. This not only confirmed that ozone cannot effectively attack OA, but also validated its structural stability at low pH value. In N3C-1100 catalytic ozonation, the ozone consumption rate increased to 36% at 5 min, and gradually decreased to 20% at 30 min and 10% at 60 min. The variation of ozone consumption rate suggested higher amount of ozone was utilized for OA removal in the first stage, and less ozone was consumed later, corresponding to slower removal rate of OA. In OA degradation profiles, the degradation rate was higher within the first 20 min and then gradually decreased, which was quite in line with the ozone consumption rates variations. For RGO/O₃ catalytic system, a slightly greater ozone consumption rate was observed, suggesting more ozone molecules were decomposed. It should be mentioned that the short residence time of ozone in the semi-batch reactor resulted in a low consumption rate.



Based on the above discussion, N-doped nanocarbon (N3C-1100) induces an OA destruction pathway both involving O₃ dissociation products based on direct surface oxidation and the ·OH based pathway. Our DFT calculations and *in situ* Raman measurements suggested that O₃ molecules tended to catalytically dissociate into O_{ad}^{*} and O_{2 free}^{*} on the active sites (Eq. 1). The redistribution of charge density induced by the high electronegativity of doped N might influence the electron transfer processes and inhibit subsequent radical chain reactions for the formation of radicals such as HO₂[·] and ·OH. This speculation was validated by EPR analysis and H₂O₂ detection results in Fig. 5C and 5D, respectively. As shown in Eq. 2, owing to the strong oxidation potential of the dissociated oxygen atoms [25], O_{ad}^{*} on the N-doping sites or the adjacent C atoms with a high charge density could directly attack adsorbed OA molecules, and it may also be protonated by ambient water to form a ·OH on the catalyst's surface (·OH_{ad}), contributing to OA destruction (Eq. 3) [25]. These direct oxidation pathways might enhance the ozone utilization efficiency. O_{ad}^{*} might also be protonated by ambient water molecules and desorbed from the surface to form ·OH (Eq. 4), which is possibly responsible for the destruction of free OA molecules in solution. In addition, O_{2 free}^{*} could be transformed into HO₂[·]/O₂^{·-} and further react with O₃ to form ·OH (Eq. 5).

4. Conclusions

In summary, we developed a facile protocol for synthesizing N-doped metal-free catalysts with high activities and robust structures by employing β-CD as a C precursor and melamine as a N precursor. Compared with undoped CD-1100, N-doping resulted in a significant enhancement of the catalytic performance. DFT simulations together with material characterization demonstrated the crucial effects of N-doping sites (especially quaternary N) on the catalytic dissociation of ozone. Moreover, the C atoms adjacent to the N-doping sites also exhibited high affinities for O₃ decomposition owing to a dense charge density. This N-doped nanocarbon exhibited a surface oxidation pathway induced by O_{ad}^{*} for OA destruction in addition to ·OH-based

reactions. O_{ad}^{*} and O_{2 free}^{*} could subsequently evolve to ·OH on the surface or in bulk solution, thus further contributing to OA destruction. This study advanced the understanding of the reaction mechanisms involved in catalytic ozonation over N-doped nanocarbons. However, further efforts are still required to elucidate the evolution of the O₃ dissociation intermediates.

Conflicts of interest

There are no conflicts to declare.

Acknowledgements

This work was supported by the National Science Fund for Distinguished Young Scholars of China (No. 51425405), the National Natural Science Foundation of China (No. 21606253), the Science Foundation of China University of Petroleum, Beijing (No. 2462016YJRC013), the Beijing Natural Science Foundation (No. 8172043), and Independent Project of the State Key Laboratory of Petroleum Pollution Control, CNPC Research Institute of Safety and Environmental Technology (No. 2017004).

Appendix A. Supplementary data

Supplementary material related to this article can be found, in the online version, at doi:<https://doi.org/10.1016/j.apcatb.2019.05.008>.

References

- [1] B. Kasprzyk-Hordern, M. Ziółek, J. Nawrocki, Appl. Catal. B 46 (2003) 639–669.
- [2] J. Nawrocki, B. Kasprzyk-Hordern, Appl. Catal. B 99 (2010) 27–42.
- [3] A.C. Mecha, M.S. Onyango, A. Ochieng, C.J.S. Fourie, M.N.B. Momba, J. Catal. 341 (2016) 116–125.
- [4] H. Cao, L. Xing, G. Wu, Y. Xie, S. Shi, Y. Zhang, D. Minakata, J.C. Crittenden, Appl. Catal. B 146 (2014) 169–176.
- [5] Y. Wang, Y. Xie, H. Sun, J. Xiao, H. Cao, S. Wang, Catal. Sci. Technol. 6 (2016) 2918–2929.
- [6] S. Afzal, X. Quan, J. Zhang, Appl. Catal. B 206 (2017) 692–703.
- [7] P. Liu, Y. Ren, W. Ma, J. Ma, Y. Du, Chem. Eng. J. 345 (2018) 98–106.
- [8] Z. Bai, Q. Yang, J. Wang, Chem. Eng. J. 300 (2016) 169–176.
- [9] Y. Guo, B. Xu, F. Qi, Chem. Eng. J. 287 (2016) 381–389.
- [10] H. Ba, Y. Liu, L. Truong-Phuoc, C. Duong-Viet, J.-M. Nhut, D.L. Nguyen, O. Ersen, G. Tuci, G. Giambastiani, C. Pham-Huu, ACS Catal. 6 (2016) 1408–1419.
- [11] J. Xiao, J. Rabeh, J. Yang, Y. Xie, H. Cao, A. Brückner, ACS Catal. 7 (2017) 6198–6206.
- [12] W. Qi, D. Su, ACS Catal. 4 (2014) 3212–3218.
- [13] X. Duan, H. Sun, S. Wang, Acc. Chem. Res. 51 (2018) 678–687.
- [14] C. Tang, Q. Zhang, Adv. Mater. 29 (2017) 1604103.
- [15] J. Xi, Q. Wang, J. Liu, L. Huan, Z. He, Y. Qiu, J. Zhang, C. Tang, J. Xiao, S. Wang, J. Catal. 359 (2018) 233–241.
- [16] M. Yang, N. Zhang, Y. Wang, Y. Xu, J. Catal. 346 (2017) 21–29.
- [17] Y. Wang, H. Cao, L. Chen, C. Chen, X. Duan, Y. Xie, W. Song, H. Sun, S. Wang, Appl. Catal. B 229 (2018) 71–80.
- [18] Y. Wang, Y. Xie, H. Sun, J. Xiao, H. Cao, S. Wang, ACS Appl. Mater. Interfaces 8 (2016) 9710–9720.
- [19] J. Zhang, L. Dai, ACS Catal. 5 (2015) 7244–7253.
- [20] X. Duan, K. O'Donnell, H. Sun, Y. Wang, S. Wang, Small 11 (2015) 3036–3044.
- [21] H. Sun, Y. Wang, S. Liu, L. Ge, L. Wang, Z. Zhu, S. Wang, Chem. Commun. 49 (2013) 9914–9916.
- [22] Y. Wang, H. Sun, X. Duan, H.M. Ang, M.O. Tadé, S. Wang, Appl. Catal. B 172–173 (2015) 73–81.
- [23] Y. Wang, H. Cao, C. Chen, Y. Xie, H. Sun, X. Duan, S. Wang, Chem. Eng. J. 355 (2019) 118–129.
- [24] T. Zhang, J.-P. Croué, Appl. Catal. B 144 (2014) 831–839.
- [25] J. Bing, C. Hu, L. Zhang, Appl. Catal. B 202 (2017) 118–126.
- [26] T. Zhang, W. Li, J.-P. Croué, Environ. Sci. Technol. 45 (2011) 9339–9346.
- [27] A. Ikhlaq, S. Waheed, K.S. Joya, M. Kazmi, Catal. Commun. 112 (2018) 15–20.
- [28] Z. Liu, J. Ma, Y. Cui, B. Zhang, Appl. Catal. B 92 (2009) 301–306.
- [29] Y. Wang, Z. Ao, H. Sun, X. Duan, S. Wang, Appl. Catal. B 198 (2016) 295–302.
- [30] X. Duan, H. Sun, Z. Shao, S. Wang, Appl. Catal. B 224 (2018) 973–982.
- [31] P. Hu, H. Su, Z. Chen, C. Yu, Q. Li, B. Zhou, P.J.J. Alvarez, M. Long, Environ. Sci. Technol. 51 (2017) 11288–11296.
- [32] M.V. Rekharsky, Y. Inoue, Chem. Rev. 98 (1998) 1875–1918.
- [33] S. Lebedkin, P. Schweiss, B. Renker, S. Malik, F. Henrich, M. Neumaier, C. Stoermer, M.M. Kappes, Carbon 40 (2002) 417–423.
- [34] S. Yan, Z. Li, Z. Zou, Langmuir 25 (2009) 10397–10401.
- [35] A.G. Bhavani, W.Y. Kim, J.S. Lee, ACS Catal. 3 (2013) 1537–1544.

- [36] D. Wei, Y. Liu, L. Cao, L. Fu, X. Li, Y. Wang, G. Yu, D. Zhu, *Nano Lett.* 6 (2006) 186–192.
- [37] D. Wei, Y. Liu, Y. Wang, H. Zhang, L. Huang, G. Yu, *Nano Lett.* 9 (2009) 1752–1758.
- [38] X. Duan, Z. Ao, H. Sun, S. Indrawirawan, Y. Wang, J. Kang, F. Liang, Z.H. Zhu, S. Wang, *ACS Appl. Mater. Interfaces* 7 (2015) 4169–4178.
- [39] D. Deng, X. Pan, L. Yu, Y. Cui, Y. Jiang, J. Qi, W.-X. Li, Q. Fu, X. Ma, Q. Xue, G. Sun, X. Bao, *Chem. Mater.* 23 (2011) 1188–1193.
- [40] L. Čirić, A. Sienkiewicz, R. Gaál, J. Jaćimović, C. Váju, A. Magrez, L. Forró, *Phys. Rev., B Condens. Matter* 86 (2012) 195139.
- [41] S. Lee, H. Lee, J.H. Sim, D. Sohn, *Macromol. Res.* 22 (2014) 165–172.
- [42] Y. Gao, Y. Zhu, L. Lyu, Q. Zeng, X. Xing, C. Hu, *Environ. Sci. Technol.* (2018).
- [43] Z. Sheng, L. Shao, J. Chen, W. Bao, F. Wang, X. Xia, *ACS Nano* 5 (2011) 4350–4358.
- [44] X. Li, H. Wang, J.T. Robinson, H. Sanchez, G. Diankov, H. Dai, *J. Am. Chem. Soc.* 131 (2009) 15939–15944.
- [45] J. Xiao, Y. Xie, F. Nawaz, S. Jin, F. Duan, M. Li, H. Cao, *Appl. Catal. B* 181 (2016) 420–428.
- [46] N. Hasty, P.B. Merkel, P. Radlick, D.R. Kearns, *Tetrahedron Lett.* 13 (1972) 49–52.
- [47] K. Ogino, N. Kodama, M. Nakajima, A. Yamada, H. Nakamura, H. Nagase, D. Sadamitsu, T. Maekawa, *Free Radical Res.* 35 (2001) 735–747.
- [48] D.B. Mawhinney, B.J. Vanderford, S.A. Snyder, *Environ. Sci. Technol.* 46 (2012) 7102–7111.
- [49] F.J. Benítez, J.L. Acero, F.J. Real, G. Roldán, E. Rodríguez, *J. Hazard. Mater.* 282 (2015) 224–232.
- [50] Y. Sun, J.J. Pignatello, *Environ. Sci. Technol.* 29 (1995) 2065–2072.
- [51] T.M. El-Morsi, W.R. Budakowski, A.S. Abd-El-Aziz, K.J. Friesen, *Environ. Sci. Technol.* 34 (2000) 1018–1022.
- [52] S. Inoue, S. Kawanishi, *Biochem. Biophys. Res. Commun.* 159 (1989) 445–451.
- [53] M. Wei, L. Gao, J. Li, J. Fang, W. Cai, X. Li, A. Xu, *J. Hazard. Mater.* 316 (2016) 60–68.
- [54] H. Lee, H.-i. Kim, S. Weon, W. Choi, Y.S. Hwang, J. Seo, C. Lee, J.-H. Kim, *Environ. Sci. Technol.* 50 (2016) 10134–10142.
- [55] W. Li, G.V. Gibbs, S.T. Oyama, *J. Am. Chem. Soc.* 120 (1998) 9041–9046.
- [56] R. Radhakrishnan, S.T. Oyama, *J. Catal.* 199 (2001) 282–290.
- [57] J. Bing, C. Hu, Y. Nie, M. Yang, J. Qu, *Environ. Sci. Technol.* 49 (2015) 1690–1697.
- [58] L.A. Sternberger, P.H. Hardy, J.J. Cuculis, H.G. Meyer, *J. Histochem. Cytochem.* 18 (1970) 315–333.